

A 3D Non-Stationary Wideband Massive MIMO Channel Model Based on Ray-Level Evolution

Carlos F. López¹, Cheng-Xiang Wang¹, *Fellow, IEEE*, and Yi Zheng, *Student Member, IEEE*

Abstract—In this paper, a novel space-time non-stationary three-dimensional (3D) wideband massive multiple-input multiple-output (MIMO) channel model is proposed. We then propose a ray-level process to model the spatial-temporal evolution of individual multipath components (MPCs), including near-field effects and (dis)appearance, and cluster-level large-scale fading. The proposed evolution process can flexibly control rays' lifespans and smoothness of (dis)appearance in both space and time domains. In addition, we propose an improved Rayleigh-distance criterion to determine the most adequate wavefront for each cluster and ray. Existing models can easily implement the proposed criterion and make a more efficient use of computation resources. Also, a Gamma-Poisson mixture distribution is introduced to model the distribution of the number of clusters when multiple locations of the mobile station are considered. Key statistical properties of the channel, including the autocorrelation function (ACF), Doppler power spectral density (PSD), spatial cross-correlation function (S-CCF), and frequency correlation function (FCF), are derived and the impact of the ray-level evolution process on them is analyzed. We demonstrate the correctness of the derived statistical properties through numerical and simulation results.

Index Terms—Massive MIMO, 3D non-stationary channel models, ray-level evolution, ray (dis)appearance, Rayleigh distance.

I. INTRODUCTION

IN THE last decade, massive multiple-input multiple-output (MIMO) technologies have been proposed as candidates for the fifth generation (5G) and sixth generation (6G) wireless communication systems [1]–[3]. In order to evaluate the

feasibility of these promising technologies, several testbeds employing a large number of antennas, e.g., tens or hundreds, have successfully been developed [4]–[6]. These have overcome the most important implementation challenges and demonstrated that massive MIMO technologies can cope with the increasing traffic demand and efficiency requirements of 5G and 6G systems.

From a practical perspective, compact-shape large antenna arrays are highly desirable as they are easier to deploy. However, key features enabled by massive MIMO technologies, e.g., large array and multiplexing gains, extreme angular resolution, and diversity, are intrinsically related to the largest dimension of the array and the separation between its elements [7], [8]. As a consequence, massive MIMO large antenna arrays are usually affected by new propagation phenomena, e.g., near-field effects and large-scale fading over the array, that were negligible in conventional MIMO wireless communication systems. Near-field effects take place when the distance between the array and the scatterers is shorter than the Rayleigh distance, which is $2D_A^2/\lambda$ with D_A denoting the largest dimension of the array and λ the carrier wavelength. It is important to note that the Rayleigh distance was derived assuming free-space line-of-sight (LoS) propagation and does not consider other phenomena related to multipath propagation [9], [10].

Massive MIMO channel measurements have demonstrated that antenna arrays spanning long distances often result in wireless channels that cannot be regarded as wide-sense stationary (WSS) [11]–[23]. Measurements employed virtual uniform linear arrays (ULAs) [11]–[16], uniform cylindrical arrays (UCAs) [11], [12], [16], and uniform planar arrays (UPAs) [16], [19]–[22] at a single frequency band, e.g., 2.6 GHz [11]–[14], and at multiple frequency bands, e.g., 11, 16, 28, and 38 GHz [19]. They demonstrated different array-varying characteristics of the channel such as angles of arrival (AOAs) and departure (AODs), propagation delays, received power, Rician K-factor, and number of propagation paths or clusters of multipath components (MPCs). Additionally, recent measurements employed advanced clustering and ray tracking algorithms to demonstrate the existence of massive MIMO effects of both clusters and individual MPCs or rays as well [21], [22].

The study and modeling of the propagation channel plays a key role in the performance assessment and design of 5G wireless communication technologies and beyond. Models capable of capturing specific characteristics of massive MIMO channels have recently been developed [24]–[39]. In particular, near-field effects were captured by employing high-order

Manuscript received August 3, 2020; revised February 11, 2021, June 9, 2021, and August 17, 2021; accepted September 23, 2021. Date of publication October 15, 2021; date of current version December 17, 2021. The authors gratefully acknowledge the support of this work from the National Key R&D Program of China under Grant 2018YFB1801101, the National Natural Science Foundation of China (NSFC) under Grants 61960206006 and 61901109, the Frontiers Science Center for Mobile Information Communication and Security, the High Level Innovation and Entrepreneurial Research Team Program in Jiangsu, the High Level Innovation and Entrepreneurial Talent Introduction Program in Jiangsu, the Research Fund of National Mobile Communications Research Laboratory, Southeast University, under Grants 2020B01 and 2021B02, the Fundamental Research Funds for the Central Universities under Grant 2242021R30001, the EU H2020 RISE TESTBED2 project under Grant 872172, and the Taishan Scholar Program of Shandong Province. The associate editor coordinating the review of this article and approving it for publication was O. Oyman. (*Corresponding author: Cheng-Xiang Wang.*)

Carlos F. López is with MathWorks, Glasgow G2 2NR, U.K. (e-mail: clopez@mathworks.com).

Cheng-Xiang Wang and Yi Zheng are with the National Mobile Communications Research Laboratory, School of Information Science and Engineering, Southeast University, Nanjing 210096, China, and also with Purple Mountain Laboratories, Nanjing 211111, China (e-mail: chxwang@seu.edu.cn; zheng_yi@seu.edu.cn).

Color versions of one or more figures in this article are available at <https://doi.org/10.1109/TCOMM.2021.3120757>.

Digital Object Identifier 10.1109/TCOMM.2021.3120757

wavefronts, e.g., spherical [24]–[27], [30]–[37], [40]–[42] or parabolic [28], [29], [38]. High-order wavefronts are computationally more complex than the simple plane wavefront as they require to calculate the exact or high-order approximations of the distances between every antenna element of the array and the surrounding scatterers. In order to determine which wavefront should be employed, the authors of previous works calculated the Rayleigh distance using the largest dimension of the array as defined above without considering clusters' lifespans over the array. In addition, they assumed that rays' lifespans over the array were equal to those of clusters. Therefore, they concluded that high-order wavefronts were required for most clusters and rays. Clearly, a more efficient use of wavefronts can be achieved.

In most massive MIMO channel models [24]–[27], [30]–[33], [35], [37], [40], large-scale fading over the array was captured focusing on the array-varying number of clusters of rays. For that purpose, birth-death (BD) processes [24]–[26], [28], [29], [31], [33], [35], [40] or visibility regions (VRs) [27], [32], [34], [37] were employed. In the BD approach, clusters (dis)appear over the array according to a random process. In the VR approach, clusters are assigned regions of the array whose location and size are randomly distributed. Thus, if a cluster is *alive* or *visible* for a particular antenna element, its rays can be transmitted (received) by that antenna. These models predict that the random number of clusters at any location of the array is Poisson distributed. However, measurements in [12] reported that a negative Binomial distribution is more accurate. How to resolve this apparent contradiction is still an open question.

Aside from cluster (dis)appearance, very few works modeled cluster-level large-scale fading over the array. In [33] and [34], the slope of the cluster-level large-scale fading was only considered. In [26], the authors included cluster-level path loss, but neglected shadow fading. Recent works added a spatial log-normal process per cluster [28], [29], but neglected the underlying ray-level (dis)appearance process that causes it. The readers are referred to [43] and [44] where the authors presented comprehensive surveys on massive MIMO and 5G channel measurements and models, respectively.

Although ray-level spherical wave propagation and (dis)appearance over the array were reported in measurements [21], [22], models including these phenomena and comprehensive studies of its impact on their statistical properties are still missing. In [37], the authors measured and modeled ray-level (dis)appearance for the mobile station side, but they neglected this phenomenon at the base station array. To fill this gap, we propose a three-dimensional (3D) non-stationary massive MIMO channel model that includes ray-level evolution and we study its effects into its small- and large-scale statistical properties. Next, we highlight the main contributions and novelties of this paper:

- 1) We propose a novel 3D non-stationary wideband massive MIMO channel model that is able to capture space-time ray-level evolution. The proposed evolution process can flexibly control rays' lifespans and smoothness of (dis)appearance in both space and time domains. Cluster-level large-scale fading is

automatically embedded in the model as a consequence of the ray-level process and smooth cluster-level (dis)appearance is guaranteed. The proposed channel model is suitable for 3D antenna-array layouts of arbitrary shape.

- 2) We propose a method to accurately determine the most adequate wavefront for each cluster and ray. This wavefront selection criterion extends the definition of Rayleigh distance and considers the lifespan of rays and clusters to calculate an effective Rayleigh distance. We prove that the number of rays that require spherical wavefronts can be greatly reduced by employing the proposed method.
- 3) We derive key statistical properties of the ray-level evolution process and study the impact of its parameters on the statistical properties of the massive MIMO channel model. We demonstrate the correctness of our derivations through simulations.
- 4) We propose a Gamma-Poisson mixture distribution to model the number of clusters when multiple locations of the mobile station are considered. This model solves the apparent contradiction between previous channel measurements and models in order to fit the distribution of the random number of clusters appropriately.

The rest of this paper is organized as follows. In Section II, we introduce the proposed 3D massive MIMO channel model including the ray-level evolution process and the improved ray-level wavefront-selection method. We derive the statistical properties of the channel model, study the impact of the ray evolution process on them and introduce the Gamma-Poisson mixture distribution to model the number of clusters in Section III. In Section IV, we study the statistical properties of the channel model through numerical and simulation results and verify the correctness of our derivations. Finally, conclusions are drawn in Section V.

II. A WIDEBAND MASSIVE MIMO CHANNEL MODEL

Let us consider a generic 3D wireless channel in which the transmitter (Tx) and receiver (Rx) can be equipped with arbitrary-shaped 3D antenna arrays. For simplicity, we assume that only the Rx is equipped with a large number of antennas. The p -th ($p = 1, 2, \dots, N_T$) transmitting and q -th ($q = 1, 2, \dots, N_R$) receiving omnidirectional antenna elements are denoted as A_p^T and A_q^R , respectively. The position vector and distance of the antenna A_p^T (A_q^R) measured from the center of the transmitting (receiving) array are denoted as \mathbf{a}_p^T (\mathbf{a}_q^R) and $\delta_p^T = \|\mathbf{a}_p^T\|$ ($\delta_q^R = \|\mathbf{a}_q^R\|$), respectively, with $\|\cdot\|$ denoting the Euclidian norm. We assume that the Tx (Rx) moves with a velocity \mathbf{v}^T (\mathbf{v}^R) of constant magnitude v^T (v^R). Scattered rays with similar parameters, e.g., AOA, AODs, and delays, are grouped into C clusters composed of N_m , $m = 1 \dots C$, rays each. In the following, the n -th scatterer of the m -th cluster is denoted as S_{mn} and its position vector measured from the center of the transmitting (receiving) array is denoted as \mathbf{s}_{mn}^T (\mathbf{s}_{mn}^R). The azimuth and zenith AODs (AOAs) of the scattered rays are denoted as ϕ_{mn}^T (ϕ_{mn}^R) and θ_{mn}^T (θ_{mn}^R), respectively. The most important elements of the channel model are depicted in Fig 1. For illustration purposes, we have

B. Spherical Wavefront vs. Plane Wavefront

The total length of the path from A_p^T to A_q^R via the first scatterer S_{mn}^T and the last scatterer S_{mn}^R used in (2) and (3) can be calculated as $D_{mn,qp}(t) = D_{mn,p}^T(t) + D_{mn,q}^R(t) + D_{mn,s}$, i.e.,

$$D_{mn,qp}(t) = \left\| \mathbf{s}_{mn}^T - \mathbf{a}_p^T - \mathbf{v}^T \cdot t \right\| + \left\| \mathbf{s}_{mn}^R - \mathbf{a}_q^R - \mathbf{v}^R \cdot t \right\| + D_{mn,s} \quad (5)$$

where the term $D_{mn,s}$ denotes the propagation distance between the first and last scatterers. Clearly, for single-bounced signals $S_{mn}^R = S_{mn}^T = S_{mn}$ and $D_{mn,s} = 0$ (see Fig. 1). However, due to the lack of information, multi-bounce scattering is usually abstracted as a virtual link between the first and last bounces. The conventional approximation for short periods of time and small arrays, i.e., the first-order or plane-wavefront approximation, reduces the distance in (5) to [29]

$$D_{mn,qp}(t) \approx D_{mn} - \delta_p^T \cos \psi_{mn}^T - \delta_q^R \cos \psi_{mn}^R - \mathbf{v}^T t \cos \xi_{mn}^T - \mathbf{v}^R t \cos \xi_{mn}^R \quad (6)$$

where D_{mn} is propagation distance from the center of the transmitting array to the center of the receiving array via S_{mn} . The angles ψ_{mn}^T , and ξ_{mn}^T can be easily obtained as

$$\cos \psi_{mn,p}^T = \frac{\mathbf{a}_p^T \cdot \mathbf{s}_{mn}^T}{\|\mathbf{a}_p^T\| \cdot \|\mathbf{s}_{mn}^T\|} \quad (7)$$

$$\cos \xi_{mn}^T = \frac{\mathbf{v}^T \cdot \mathbf{s}_{mn}^T}{\|\mathbf{v}^T\| \cdot \|\mathbf{s}_{mn}^T\|}. \quad (8)$$

The explicit dependency of the angles $\psi_{mn,p}^T$ and ξ_{mn}^T with respect to the azimuth and elevation AODs can be seen in spherical coordinates as

$$\cos \psi_{mn,p}^T = \sin \theta_{mn}^T \sin \beta_p^T \cos(\phi_{mn}^T - \alpha_p^T) + \cos \theta_{mn}^T \cos \beta_p^T \quad (9)$$

$$\cos \xi_{mn}^T = \sin \theta_{mn}^T \sin \beta_v^T \cos(\phi_{mn}^T - \alpha_v^T) + \cos \theta_{mn}^T \cos \beta_v^T \quad (10)$$

where the terms α_p^T and β_p^T denote the azimuth and elevation components of A_p^T with respect to the center of the transmitting array. Similarly, the terms α_v^T and β_v^T denote the azimuth and elevation components of the velocity vector \mathbf{v}^T , respectively. The angles $\psi_{mn,q}^R$ and ξ_{mn}^R are analogously obtained and are omitted here. In conventional WSS models [45], the plane-wavefront approximation in (6) is used to calculate the phase of the signal in (2) and (3). However, this first-order polynomial in δ_p^T , δ_q^R , and t results in linear spatial-temporal variations of the phase that do not capture the non-stationary properties of massive MIMO channels. In such case, the AODs and AOA are implicitly assumed to be constant over the array and time. Moreover, the delay $\tau_{mn,qp}(t)$ in (2) is usually approximated as a constant value for every path, i.e., $\tau_{mn,qp}(t) = \tau_{mn}$. However, this may be incorrect for large arrays and long periods of time as it has been recently shown in [46].

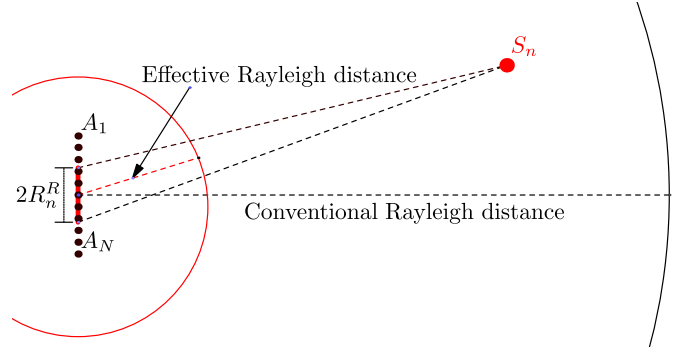


Fig. 2. Comparison of the conventional Rayleigh distance calculated using the largest dimension of the array (black) and the proposed effective Rayleigh distance considering the ray's VR (red). The ray's lifespan is depicted as a red segment over the array.

C. Adaptive Wavefronts Using the Effective Rayleigh Distance

One of the advantages of the proposed ray-level process is the possibility of selecting the appropriate wavefront for each ray. The parameter commonly used to determine which wavefront is required is the Rayleigh distance, which is $D_R = 2D_A^2/\lambda$ with D_A denoting the largest dimension of the array and λ the carrier wavelength. However, as most clusters and rays only exist over very small regions of the array [20]–[22], their effective Rayleigh distance is smaller than D_A . We define the effective Rayleigh distance of a ray as $D_{E,n} = 2(2R_n^R)^2/\lambda$ with R_n^R the radius of the ray's VR, i.e., $2R_n^R$ is the ray's lifespan over the array. Thus, when a scatterer is located at a distance $r_n > D_{E,n}$ measured from the center of the ray's VR, plane wavefronts can be appropriately used. Fig. 2 illustrates the concept of effective Rayleigh distance using a ULA. Note that halving the radius of the ray's VR makes the effective Rayleigh distance four times shorter. The same concept can be applied to the time domain for which the effective Rayleigh distance is calculated as $2(v^R \cdot T_n^R)^2/\lambda$ with $T_n^R = 2R_n^R/v^R$, where we assumed the Rx moves at a constant speed v^R across the ray's VR.

Measurements in [21], [22] have shown that R_n^R can accurately be approximated using i.i.d. exponentially distributed random variables of equal rate λ^R . Thus, for a particular cluster of scatterers located at distance r_0 , it can be seen that the average ratio of the number N_R^{SW} of scatterers that require spherical wavefronts to the total number N_R of scatterers is $N_R^{\text{SW}}/N_R = \exp(-\sqrt{r_0/\bar{r}_R})$. The parameter \bar{r}_R denotes the effective Rayleigh distance of an average-size ray's VR, which is given by $\bar{r}_R = 16(\bar{R}^R)^2/\lambda$ with $\bar{R}^R = 1/\lambda^R$ denoting the average radius of the rays' VRs. Note that for an average ray's lifespan which is 4 times shorter than the largest dimension of the array, i.e., $D_A/\bar{R}^R = 8$, less than 3% of the rays would require spherical wavefronts to be employed. Analogous conclusions apply to the clusters since the radius of the cluster's VR is exponentially distributed as well [21], [22]. However, as clusters' lifespans are larger in average than rays' lifespans, the clusters that require spherical wavefronts may be larger.

In order to reduce the computational complexity, the following procedure is used with those scatterers located beyond their

effective Rayleigh distance. First, we use (5) to calculate the exact distance traveled by the scattered ray only at the center of the ray's VR. Second, we use (6) to obtain the approximate distance traveled by rays received within the VR. This is in contrast with previous approaches, in which the exact distance in (5) was used for every ray, antenna element of the array and time instant. This method enables to reduce the computational burden of the wavefront computation process by the ratio of the complexity of computing the spherical wavefront to that of the plane wavefront.

For practical communication scenarios such as rural macrocell, in which cells are deployed over wide areas, users are often far from the base station, and clutter is more sparse, the number of rays that require spherical wavefronts can be significantly lower and their lifespan longer than those in smaller deployments such as urban microcell, indoor hotspot, and indoor factory.

III. STATISTICAL PROPERTIES OF THE CHANNEL MODEL

In this section, we will study key statistical properties of the proposed massive MIMO channel model. Although we will mainly focus on the small-scale properties, some relevant characteristics of the large-scale fading will be studied as well. As we will study the cluster-level statistical properties of the channel, we will drop the cluster index m in the following sections when it is not essential for the sake of notation simplicity and readability.

A. Small-Scale Fading

1) *Distribution of the Amplitude of Rays*: Measurements in [21], [22] indicate that the time of arrival t_n , with $n = 1, 2, \dots, N$, of rays within a cluster can be modeled as i.i.d. random variables uniformly distributed over the interval $(0, T_C]$. The cluster and rays within it remain visible over periods of time denoted as T_C and T_n^R , respectively. The rays' lifetimes T_n^R can be modeled as i.i.d. exponential random variables of equal rate $\lambda^R = \lambda_n^R$ as indicated in [21], [22]. Thus, the probability distribution function (PDF) of the amplitude of the rays can be obtained using the theory of transformation of random variables as

$$p_{g_n(t)}(x) = (1 - p_v) \delta(x) + p_v \left(\frac{r}{\pi \sqrt{c_n x - x^2}} + (1 - r) \delta(x - c_n) \right) \quad (11)$$

for $0 \leq x \leq c_n$ and zero otherwise. The term $p_v = (\lambda^R T_C)^{-1}$ denotes the probability of a ray being visible at any time t of the cluster's lifetime. Hence, the first term $(1 - p_v)$ in (11) denotes the probability of the amplitude of the ray being zero, i.e., scatterer not visible. The second term corresponds to the transition period of (dis)appearance and the third to the period of maximum amplitude c_n . Eq. (11) is approximately time invariant in $(\lambda^R)^{-1} < t \leq T_C - (\lambda^R)^{-1}$ and is time dependent outside this interval. As the average ray's lifetime of a ray is much smaller than that of a cluster [21], [22], i.e., $T_C \lambda^R \gg 1$, the distribution can be approximated by (11) and $g_n(t)$ can be considered as a first-order stationary process. Note that the time-varying distribution of the amplitude of rays (11) at the

edges of a cluster lifespan ensures that there are no sudden transitions when a cluster (dis)appears.

The PDF of the amplitude of the rays in the spatial domain is given by

$$p_{g_n(\mathbf{r}^R)}(x) = (1 - p_v) \delta(x) + p_v \frac{(2\pi r_0 + r \arccos(1 - 2x))^2}{2\pi^2 \sqrt{c_n x - x^2}} + p_v (1 - r) \delta(x - c_n) \quad (12)$$

where the probability of a ray being visible at any location is $p_v = 4\pi(\bar{R}^R)^3 / (L'_x L'_y L'_z)$. The parameters L'_x , L'_y , and L'_z denote the x , y , and z dimensions, respectively, of a region containing the large array where the rays' VRs are randomly generated according to a uniform distribution.

2) *Distribution of the Envelope*: Next, we will study the effects of the ray-level gain on the distribution of the cluster-level envelope process $\Xi = |h_{m,qp}(t)|$ in (2) only in the temporal domain as closed-form expressions can be derived. The analysis in the spatial domain leads to closed-form expressions only in the case of ULAs, but it is more complex for 3D antenna arrays of arbitrary shape. The distribution of Ξ for a fixed time instant t is given by (see Appendix)

$$p_{\Xi}(z) = (2\pi)^2 z \int_0^{\infty} \exp \left\{ r N_a {}_2F_3 \left(\frac{1}{4}, \frac{3}{4}; \frac{1}{2}, 1, 1; -(c\pi x)^2 \right) \right\} \times \exp \{ N_a [J_0(2\pi c x)(1 - r) - 1] \} J_0(2\pi z x) x dx \quad (13)$$

for $z > 0$, with ${}_2F_3(\cdot; \cdot; \cdot)$ denoting the generalized hypergeometric series of order 2, 3 [47] and N_a the average number of active rays within the cluster at any time instant. Note that all the rays are assumed to have the same maximum amplitude $c = c_n$ in (13). For large values of N_a , the integrand of the previous expression decreases very rapidly. Thus, approximating the exponent by a third-order Taylor polynomial at $x = 0$, $p_{\Xi}(z)$ is approximately

$$p_{\Xi}(z) \approx (2\pi)^2 z \int_0^{\infty} \exp \left[-N_a (c\pi x)^2 \left(1 - \frac{5}{8} r \right) \right] \times J_0(2\pi z x) x dx. \quad (14)$$

Let σ be the total received power and the maximum amplitude of all rays is $c = \sigma \left[\frac{N_a}{2} \left(1 - \frac{5}{8} r \right) \right]^{-\frac{1}{2}}$. Finally, the previous integral can be solved using [47, Equation (6.631.4)] as

$$p_{\Xi}(z) \approx \frac{z}{\sigma^2} \exp \left(-\frac{z^2}{2\sigma} \right) \quad (15)$$

for $z > 0$ and zero otherwise. That is, the envelope is approximately Rayleigh distributed. The maximum amplitude of the rays $c = \sigma \left[\frac{N_a}{2} \left(1 - \frac{5}{8} r \right) \right]^{-\frac{1}{2}}$ depends on the average number of rays and the transition parameter r . The dependence on r compensates the effective reduction of amplitude caused by the taper. The rays' lifetimes have no effect on the distribution of the envelope as long as the average number of rays N_a remains constant over the cluster's lifetime. Note that when the average number of rays is small ($N_a < 10$), e.g., in millimeter wave channels, we have empirically determined that the previous approximation is not valid, and the amplitude is not Rayleigh distributed. In addition, for rays of non-constant amplitude, i.e., $c \neq c_n$, the distribution of the envelope can be obtained by

evaluating (45) and it cannot be approximated by a Rayleigh distribution. However, this provides an additional degree of freedom that allows for flexibility to model other distributions at the expense of higher complexity.

In the spatial domain, the analysis is analogous by plugging (12) instead of (11) into (42). Unlike in the temporal analysis, no closed-form solution has been found to such distribution for the 3D spatial ray gain.

3) Temporal Autocorrelation Function (ACF):

The normalized temporal ACF of the CIR can be defined as $\rho_{qp}(t_1, t_2) = \mathbb{E}[H_{qp}(t_1, f)H_{qp}^*(t_2, f)] / \mathbb{E}[|H_{qp}(t, f)|^2]$, where

$$\begin{aligned} & \mathbb{E}[H_{qp}(t_1, f)H_{qp}^*(t_2, f)] \\ &= \sum_{m=1}^C \sum_{m'=1}^C \sum_{n=1}^N \sum_{n'=1}^N a_m a_{m'}^* \\ & \quad \times \mathbb{E}[g_{mn,qp}(t_1 - t_{mn})g_{m'n',qp}(t_2 - t_{m'n'})] \\ & \quad \times \mathbb{E}[e^{jk_0[D_{mn,qp}(t_1) - D_{m'n',qp}(t_2)]}] \mathbb{E}[e^{j(\theta_{mn} - \theta_{m'n'})}]. \end{aligned} \quad (16)$$

Since $\mathbb{E}[e^{j(\theta_{mn} - \theta_{m'n'})}] = 1$ for $m = m'$ and $n = n'$ and is zero otherwise, then

$$\mathbb{E}[H_{qp}(t_1, f)H_{qp}^*(t_2, f)] = \sum_{m=1}^C |a_m|^2 \rho_{m,qp}(t_1, t_2) \quad (17)$$

with

$$\begin{aligned} \rho_{m,qp}(t_1, t_2) &= \sum_{n=1}^N \mathbb{E}[g_{mn,qp}(t_1 - t_{mn})g_{mn,qp}(t_2 - t_{mn})] \\ & \quad \times \mathbb{E}[e^{jk_0[D_{mn,qp}(t_1) - D_{mn,qp}(t_2)]}]. \end{aligned} \quad (18)$$

That is, the total ACF is a weighed sum of the cluster-level ACFs. The total received power can be obtained as $\mathbb{E}[|H_{qp}(t, f)|^2] = \sum_{m=1}^C |a_m|^2 \sum_{n=1}^N \mathbb{E}[|g_{mn,qp}(t - t_{mn})|^2]$,

where the received power corresponding to a single ray is given by $P_R = \mathbb{E}[|g_{mn,qp}(t - t_{mn})|^2] = c^2 (1 - \frac{5r}{8}) T^R / T_C$ for rays of constant lifetime $T_n^R = T^R$ and $P_R = c^2 (1 - \frac{3r}{4}) / (T_C \lambda^R)$ when T_n^R are modeled as exponential random variables of rate λ^R . In the calculation of P_R , the boundary effects caused at the extremes of the cluster's lifetime have been neglected.

Due to the complexity and lack of closed-form expressions of the ray-level gain ACF when T_n^R are random variables, we will derive the ACF for a constant lifetime and study its impact on the ACF of the channel. The ACF considering i.i.d. exponentially distributed rays' lifetimes will be studied numerically in Section IV. For constant T^R , the ACF of the ray gain can be obtained as $\rho_{g_n g_n}(t_1, t_2) = \mathbb{E}[g_{n,qp}(t_1 - t_n)g_{n,qp}(t_2 - t_n)] / \mathbb{E}[|g_{n,qp}(t - t_n)|^2]$, where we have dropped the cluster index m for clarity. Thus, equation (19), as shown at the bottom of the page, and zero otherwise. To simplify notation, we have used $\tau' = |t_2 - t_1|(T^R)^{-1}$, $\tau'' = \tau' - 1$. Equation (19) is valid only for $0 \leq \tau' \leq 2/3$. For $2/3 < \tau' \leq 1$ the ACF is obtained as (20), shown at the bottom of the page.

As we have shown in (11), the ray gain is a first-order stationary process in the interval $T^R/2 < t < T_C - T^R/2$. As the ACFs in (19) and (20) depend only on the time difference $|t_2 - t_1|$ for $T^R/2 < t_i < T_s - T^R/2$ with $i = 1, 2$, the process is also second-order stationary and hence WSS for the majority of the cluster's lifetime. Assuming that the amplitudes of the rays are constant $c_n = \sigma[\frac{N}{2}(1 - \frac{5}{8}r)]^{-1/2}$, the cluster-level temporal ACF is given by

$$\begin{aligned} \rho_{qp}(t_1, t_2) &= \frac{1}{N} \sum_{n=1}^N \rho_{g_n g_n}(t_1, t_2) \\ & \quad \times \mathbb{E}[e^{jk_0[D_{n,qp}(t_1) - D_{n,qp}(t_2)]}]. \end{aligned} \quad (21)$$

When all the rays' lifetimes are equal or they are equally i.i.d. random variables, this ACF can be separated as

$$\rho_{g_n g_n}(\tau') = \begin{cases} \frac{1}{8-5r} \left[8 - 6r - 4\tau' + (r - 2\tau') \cos\left(\frac{2\pi}{r}\tau'\right) + \frac{3}{\pi}r \sin\left(\frac{2\pi}{r}\tau'\right) \right] & 0 < \tau' \leq r/2 \\ \frac{1}{1 - \frac{5}{8}r} \left[1 - \frac{1}{2}r - \tau' \right] & r/2 \leq \tau' \leq (1-r) \\ \frac{1}{8-5r} \left[6\tau'' + 2r + [\tau'' + r] \cos\left(\frac{2\pi}{r}\tau''\right) - \frac{3}{2\pi}r \sin\left(\frac{2\pi}{r}\tau''\right) \right] & (1-r) \leq \tau' \leq (1 - \frac{r}{2}) \\ \frac{1}{8-5r} \left[-\tau'' \left[2 + \cos\left(\frac{2\pi}{r}\tau''\right) \right] + \frac{3}{2\pi}r \sin\left(\frac{2\pi}{r}\tau''\right) \right] & (1-r/2) \leq \tau' \leq 1 \end{cases} \quad (19)$$

$$\rho_{g_n g_n}(\tau) = \begin{cases} \frac{1}{8-5r} \left[8 - 6r - 4\tau' + (r - 2\tau') \cos\left(\frac{2\pi}{r}\tau'\right) + \frac{3}{\pi}r \sin\left(\frac{2\pi}{r}\tau'\right) \right] & 0 < \tau' \leq 1-r \\ \frac{1}{8-5r} \left[4(1-r) - 2\tau'' + (\tau'' + r) \cos\left(\frac{2\pi}{r}\tau''\right) - \frac{3}{2\pi}r \sin\left(\frac{2\pi}{r}\tau''\right) \right] & 1-r \leq \tau' \leq r/2 \\ \frac{1}{8-5r} \left[-6\tau'' + 2r + (\tau'' + r) \cos\left(\frac{2\pi}{r}\tau''\right) - \frac{3}{2\pi}r \sin\left(\frac{2\pi}{r}\tau''\right) \right] & r/2 \leq \tau' \leq 1-r/2 \\ \frac{1}{8-5r} \left[-\tau'' \left(\cos\left(\frac{2\pi}{r}\tau''\right) + 2 \right) + \frac{3}{2\pi}r \sin\left(\frac{2\pi}{r}\tau''\right) \right] & (1-r/2) \leq \tau' \leq 1. \end{cases} \quad (20)$$

$\rho_{qp}(t_1, t_2) = \rho_{g_n g_n}(t_1, t_2) \cdot \rho_{S, qp}(t_1, t_2)$, where

$$\rho_{S, qp}(t_1, t_2) = \frac{1}{N} \sum_{n=1}^N \mathbb{E}[e^{jk_0[D_{n, qp}(t_1) - D_{n, qp}(t_2)]}] \quad (22)$$

is defined as the ACF of the cluster without ray-level evolution process. The rays' gains introduce several effects in the total ACF that are worth studying. First, as the ACF of $g_n(t)$ is a decreasing function of the time difference, the total ACF is tapered off. This effect is more important when the rays' lifetimes are of the same order of magnitude as the coherence time of the cluster, defined as $\min_{|t_2 - t_1|} [\rho_{qp}(t_1, t_2) < \rho_C]$, with $|\rho_C| \leq 1$. An estimate of the rays' lifetimes guaranteeing that the reduction of the absolute value of the ACF is at most $1/\rho_0$ with $0 < \rho_0 \leq 1$ for a time difference $|t_2 - t_1|$ can be calculated as

$$T^R = \frac{1 - (\frac{1}{2}r + \rho_0(1 + \frac{5}{8}r))}{T_C}. \quad (23)$$

This expression is valid for $r < 2/3$ and $rT^R/2 < T_C$, which are reasonable conditions as rays' lifetimes are shorter than clusters' and we assume a short (dis)appearance times.

The ACF derived above considered a constant ray's lifetime T^R for all rays. However, when T_n^R are i.i.d. random variables, the law of total probabilities can be used as

$$\rho_{g_n g_n}(\tau)(x) = \int_0^\infty \rho_{g_n g_n}(\tau)(x | T^R = y) p_{T^R}(y) dy \quad (24)$$

where $\rho_{g_n g_n}(\tau)(x | T^R = y)$ denotes the ACF of the n -th ray's gain when its lifetime is a constant value $T^R = y$ as given by (19) and (20). For exponentially distributed i.i.d. random rays' lifetimes [21], [22], the closed-form solution to (24) is $\rho_{g_n g_n}(\tau) = \exp(-\tau/\lambda^R)$, which is valid only for $r = 0$. Although we have not found a general closed-form solution to the integral above valid for any value of r , the following approximation

$$\hat{\rho}_{g_n g_n}(\tau) = e^{-\lambda^R(1+3r/8)\tau} \quad (25)$$

has been found to fit very well the results obtained using (24) for $0 < r < 1$. Thus, it can be seen that the exponentially distributed i.i.d. rays' lifetimes transform a linear decay into an exponential one. In addition, whereas the average ray's lifetime has a large effect on the total ACF, taper parameter has a relatively small impact on it.

4) *Doppler PSD*: The Doppler spectrum of the channel can be obtained as the Fourier transformation of the ACF of the CIR with respect to the time difference. As we have shown in (22), the cluster-level ACF is separable as a product of two different ACFs. By the convolution property of the Fourier transform, the cluster-level Doppler PSD can be obtained as

$$S_{qp}(\nu) = S_{g_n}(\nu) \otimes S_{S, qp}(\nu) \quad (26)$$

where ν denotes the Doppler frequency, \otimes the convolution operation, $S_{g_n}(\nu)$ the Doppler PSD of the n -th ray's gain and $S_{S, qp}(\nu)$ that of a cluster without ray-level evolution process. Due to the convolution, the cluster-level Doppler PSD is spread. For a constant value of T^R , the Doppler PSD $S_{g_n}(\nu)$

is given by the Fourier transform of the ACF in (19) with respect to τ as

$$\begin{aligned} S_{g_n}(\nu') &= \frac{(T^R)^2}{8\pi^2\nu'^2(\nu'^2 r^2 - 1)(\nu'^2 r^2 + 1)} [2(1 + \cos(r\pi\nu')) \\ &\quad - \cos(2\pi\nu') - \cos(2\pi\nu'(r-1)) - 2\cos(r\pi\nu'(r-2))] \end{aligned} \quad (27)$$

where $\nu' = \nu T^R$. Clearly, the rays' lifetimes and taper parameter determine the spectral characteristics of the ray-level evolution process. Whereas T^R is a scale parameter that controls the spread of the Doppler spectrum, r determines both the spread and level of spectral leakage. The average Doppler shift and spread can be calculated using the first and second derivative of the ACF with respect to the time difference $\dot{\rho}(0)$ and $\ddot{\rho}(0)$, respectively, as [45]

$$\begin{aligned} B_{qp}^{(1)}(t) &= \frac{1}{2\pi j} \cdot \frac{\dot{\rho}_{qp}(t, t)}{\rho_{qp}(t, t)} = \frac{1}{2\pi j} \frac{\dot{\rho}_{S, qp}(t, t)}{\rho_{S, qp}(t, t)} \quad (28) \\ B_{qp}^{(2)}(t) &= \frac{1}{2\pi} \sqrt{\left(\frac{\dot{\rho}_{qp}(t, t)}{\rho_{qp}(t, t)}\right)^2 - \frac{\ddot{\rho}_{qp}(t, t)}{\rho_{qp}(t, t)}} \\ &= \frac{1}{2\pi} \sqrt{\left(\frac{\dot{\rho}_{S, qp}(t, t)}{\rho_{S, qp}(t, t)}\right)^2 - \left(\frac{\ddot{\rho}_{S, qp}(t, t)}{\rho_{S, qp}(t, t)} - \frac{4\pi^2}{r(T^R)^2}\right)} \end{aligned} \quad (29)$$

where we have used the relationships $\dot{\rho}_{g_n}(t, t) = 0$ and $\ddot{\rho}_{g_n}(t, t) = \frac{4\pi^2}{r(T^R)^2}$. Equation (29) is not defined for $r = 0$ as the derivative of the ACF in (19) does not exist at $\tau = 0$. The average Doppler shift is not affected by the rays' gains, but the Doppler spread always increases. In particular, when rays' lifetimes are similar or greater than the reciprocal of the maximum Doppler frequency, the impact on the Doppler spread of the channel will be higher.

5) *Spatial Cross-Correlation Function (S-CCF)*: The S-CCF of the channel can be defined as the correlation between a signal transmitted from the antenna element A_p^T and received by A_q^R and that transmitted from $A_{p'}^T$ and received by $A_{q'}^R$ at time t and carrier frequency f . Thus, it can be expressed as $\rho_{qp, q'p'} = \mathbb{E}[H_{qp}(t, f)H_{q'p'}^*(t, f)] / \mathbb{E}[|H_{qp}(t, f)|^2]$. Similar to the derivation of the ACF, as $\mathbb{E}[e^{j(\theta_{mn} - \theta_{m'n'})}] = 1$ for $m = m'$ and $n = n'$ and is zero otherwise, then

$$\begin{aligned} &\mathbb{E}[H_{qp}(t, f)H_{q'p'}^*(t, f)] \\ &= \sum_{m=1}^C |a_m|^2 \sum_{n=1}^{N_m} \times \mathbb{E}[g_{mn, qp}(t - t_{gn})g_{mn, q'p'}(t - t_{mn})] \\ &\quad \times \mathbb{E}[e^{jk_0[D_{mn, qp}(t) - D_{mn, q'p'}(t)]]]. \end{aligned} \quad (30)$$

The S-CCF of the ray-level evolution process can analogously be defined $\rho_{S, qp} = \mathbb{E}[g_{mn, qp}(t - t_{mn})g_{mn, q'p'}(t - t_{mn})] / \mathbb{E}[|g_{mn, qp}(t - t_{mn})|^2]$. One important difference in the derivation of the ACF and S-CCF lies on the number of dimensions involved. Whereas the ACF is limited to a single dimension, i.e., time, a larger number of dimensions is required for antenna arrays at both sides of the communication link. Single or multiple-dimensional antenna arrangements usually lead to complex expressions of the S-CCF and closed-form

expressions are usually not achievable. In the case of ULAs with antenna spacing at the transmit- and receive-sides δ_T and δ_R , respectively, and multi-bounce propagation (where independence between the transmit-side and receive-side is usually assumed), the S-CCF of the ray-level process can be expressed the product of the transmit-side and receive-side S-CCFs. In these conditions, the S-CCFs of the ray-level evolution process can be easily obtained by using (19) and replacing $|t_2 - t_1|$ by $|\delta_R(q - q')|$. Due to the limitations described above, we will numerically study the S-CCF in Section IV.

6) *Frequency Correlation Function (FCF)*: The normalized FCF can be obtained as $\rho_{qp}(f_1, f_2) = \mathbb{E}[H_{qp}(t, f_1)H_{qp}^*(t, f_2)] / \mathbb{E}[|H_{qp}(t, f)|^2]$, where

$$\mathbb{E}[H_{qp}(t, f_1)H_{qp}^*(t, f_2)] = P_R \sum_{m=1}^C |a_m|^2 \sum_{n=1}^N \times e^{-j2\pi(f_1 - f_2)\tau_{mn,qp}(t)}. \quad (31)$$

As delays corresponding to individual rays depend on the antenna elements of the large array and time instant considered, the FCF is spatial-temporal variant (STV). As indicated by [46], the relatively small variation of the delays over the array enables to use a linear approximation of $\tau_{mn,qp}(t)$ as

$$\tau_{mn,qp}(t) \approx \tau_{0,mn} - \tau_q \cos \psi_{mn}^R - \tau_v^T(t) \cos \xi_{mn}^T - \tau_v^R(t) \cos \xi_{mn}^R \quad (32)$$

where $\tau_{0,mn}$ is the reference delay of the n -th ray in the m -th cluster from the transmitting to the receiving arrays centers, $\tau_v^T(t) = v^T t / c_0$ and $\tau_v^R(t) = v^R t / c_0$ denote the extra propagation delay induced by the motion of the Tx and Rx, respectively, and $\tau_q = \delta_q / c_0$ denotes the propagation delay from the center of the receiving large array to the q -th antenna element. Therefore, the terms $\tau_q \cos \psi_n^R$, $\tau_v^T(t) \cos \xi_n^T$, and $\tau_v^R(t) \cos \xi_n^R$ in (32) model the relative delay experienced by the signal radiated from A_p^T and received by A_q^R at time instant t with respect to $\tau_{0,mn}$. Note that previous models assumed a constant delay that is independent of the time instant and antenna element as $\tau_{qp,mn}(t) = \tau_{0,mn}$, since δ_p / c_0 , δ_q / c_0 , $v^T t / c_0$, and $v^R t / c_0$ are small in conventional WSS MIMO systems.

B. Large-Scale Fading

The ray-level evolution process may be physically interpreted as shadowing of individual rays produced by objects in the environment. Accordingly, the cluster-level large-scale fading is implicitly captured in this model due to the ray-level evolution process.

1) *Distribution of the Local-Average Received Power*: Even though the cluster-level average received power is a constant value $P_C = Nc^2(1 - 5/8r)T^R$, the cluster-level local-average received power is an STV random process describing the cluster-level shadow fading [48]. A sample function of the average received power can be obtained through the expectation of the instantaneous received power conditioned to a set of fixed parameters of the ray-level evolution process,

i.e., conditioned to a fixed large-scale environment, as

$$\mathbb{E}[H_{qp}(t, f)H_{qp}^*(t, f) | g_{mn,qp}(t - t_{mn})] = \sum_{m=1}^C |a_m|^2 \sum_{n=1}^{N_m} g_{mn,qp}^2(t - t_{mn}). \quad (33)$$

Thus, we can model the cluster-level large-scale fading by extending the formulation of the average received power proposed in [49] and defining the process $\gamma_{m,qp}(t)$ as [48]

$$\gamma_{m,qp}(t) = \sum_{n=1}^{N_m} g_{mn,qp}^2(t - t_{mn}). \quad (34)$$

Although large-scale fading is usually modeled employing a Lognormal distribution [45], the sum of Lognormal random variables is not Lognormal distributed [50], [51], which hinders the modeling of the total large-scale fading. Thus, Gamma distributions have been proposed as a convenient alternative to the Lognormal distribution for this purpose [52]. Let $c_{mn}^2 \sim \Gamma(k_{mn}, \theta)$, with $m = 1 \dots C$ and $n = 1 \dots N_m$, be a collection of i.i.d. Gamma-distributed random variables denoting the maximum squared amplitude of N_m rays in C clusters. Note that the collection shares the same scale parameter θ , hence we can use the summation property of i.i.d. Gamma random variables, i.e., $\sum_{n=1}^N c_{mn}^2 \sim \Gamma(\sum_{n=1}^N k_{mn}, \theta)$. For a sufficiently large average number of visible rays within a cluster, the resulting process modeling the cluster-level local-average received power is approximately Gamma-distributed as $\gamma_{m,qp}(t) \sim \Gamma(\sum_{n=1}^N k_{mn}, \theta)$.

2) *ACF of Cluster-Level Large-Scale Fading*: The ACF of the process $\gamma_{m,qp}(t)$ is obtained as

$$\rho_{\gamma_m \gamma_m}(t_1, t_2) = \sum_{n=1}^{N_m} \sum_{n'=1}^{N_m} \mathbb{E}[g_{mn,qp}^2(t_1 - t_{mn}) g_{m n',qp}^2(t_2 - t_{mn'})] \quad (35)$$

which can be analogously computed to the ACF of the ray gain in (19) and it is omitted here for brevity. As an example, closed-form expressions of this ACF can be found for rapid (dis)appearance of rays ($r = 0$) as $\lambda^R \exp(-\tau/\lambda^R)$ with $\tau = |t_2 - t_1|$. This ACF depends only on time difference $|t_2 - t_1|$ and has a form similar to that in (19) and (20), being a smoothly decreasing function of the time difference. Traditionally, the exponential profile has been widely used to fit measurement results of the ACF of the large-scale fading [45].

C. Distribution of the Random Number of Rays and Clusters

As in previous sections, let us assume that the appearance times of N rays within a cluster are modeled as i.i.d. random variables uniformly distributed over the cluster's lifetime as $t_n \sim \mathcal{U}(0, T_C)$, with $n = 1 \dots N$. In addition, rays' lifetimes T_n^R are modeled as i.i.d. exponentially distributed random variables with rate λ^R . The total number of the visible rays in the cluster at time t is a random variable which can be expressed as

$$n_R(t) = \sum_{n=1}^N \mathbb{1}_{t_n < t < t_n + T_n^R}. \quad (36)$$

The term $\mathbb{1}_{t_n < t < t_n + T_n^R}$ above denotes the indicator function, i.e., it is unity when $t_n < t < t_n + T_n^R$ and zero otherwise. For a given time instant t and a constant $T^R = T_n^R$, the event $t_n < t < t_n + T^R$ is a Bernoulli trial with probability of success given by

$$p(t) = \begin{cases} \frac{1}{T_C} \cdot \left(t + \frac{1}{2}T^R\right) & -\frac{T^R}{2} < t \leq \frac{T^R}{2} \\ \frac{T^R}{T_C} & \frac{T^R}{2} < t \leq T_C - \frac{T^R}{2} \\ \frac{1}{T_C} \left(T_C - t + \frac{1}{2}T^R\right) & T_C - \frac{T^R}{2} < t < T_C + \frac{T^R}{2} \end{cases} \quad (37)$$

where $T^R < T_C$ was assumed. Thus, the probability of a ray being visible is approximately a constant $p \approx T^R/T_C$ over the majority of the cluster's lifetime as long as $T^R \ll T_C$. However, as T_n^R is random, $p(t)$ can be computed using the law of total probabilities and is given by

$$p(t) = \begin{cases} \frac{1}{2} \frac{1}{\lambda^R T_C} \cdot e^{2\lambda^R t} \left(1 - e^{-2\lambda^R T_C}\right) & t \leq 0 \\ \frac{1}{\lambda^R T_C} \cdot \left(1 - \frac{1}{2} \left[e^{-2\lambda^R t} + e^{-2\lambda^R (T_C - t)} \right]\right) & 0 < t \leq T_C \\ \frac{1}{2} \frac{1}{\lambda^R T_C} \cdot \left(e^{-2\lambda^R (T_C - t)} - e^{-2\lambda^R t}\right) & T_C \leq t. \end{cases} \quad (38)$$

The number of visible rays at any time instant $n_R(t)$ is the sum of N Bernoulli trials, so it is Binomial distributed with parameters N and time-varying probability $p(t)$ as given by (38). However, as recent measurements [21], [22] showed that rays' lifetimes are usually much shorter than clusters', e.g., $\lambda^R T_C \approx 10$, from (38) the probability $p(t)$ can be approximated as $p = (\lambda^R T_C)^{-1}$. Thus, the number of visible rays is Binomial distributed as $n_R(t) \sim \mathcal{B}(N, (\lambda^R T_C)^{-1})$ approximately in the interval $0 < t < T_C$. Thus, the average number of visible rays in a cluster is approximately a constant value $N_R(t) = \mathbb{E}[n_R(t)] = Np(t) \approx N(\lambda^R T_C)^{-1}$.

When the cluster (dis)appears, the number of rays increases (decreases) exponentially and the raising (decay) time from (to) the $L\%$ to (from) the $(1 - L)\%$ of the total number of rays is

$$\Delta t_{L\%} = -\frac{1}{\lambda^R} \cdot \log\left(\frac{1}{100} \cdot \frac{2L}{1 - e^{-2\lambda^R T_C}}\right) \quad (39)$$

for $0 < L < 50\%$. Examples of transition periods are $\Delta t_{10\%} \approx 1.6(\lambda^R)^{-1}$, $\Delta t_{1\%} \approx 3.9(\lambda^R)^{-1}$, where we have assumed $\lambda^R T_C \gg 1$. The raising (decay) time $\Delta t_{L\%}$ guarantees a smooth transition of the cluster's power when it (dis)appears without adding additional elements to the model. In addition, as $\lambda^R T_C \gg 1$ [21], [22], the law of rare events allows us to approximate $n_R(t)$ as a Poisson random variable with rate parameter $N(\lambda^R T_C)^{-1}$, as proposed by previous non-stationary massive MIMO channel models [24]–[26].

Using an analogous argument, the number of visible clusters at any time instant $n_C(t)$ is Poisson distributed with rate parameter λ^C . However, measurements [12] reported that

the number of clusters at different locations of the array can be accurately modeled by a negative binomial random variable when multiple locations of the mobile station (MS) are considered. This apparent contradiction is solved by noting that a negative binomial distribution can be obtained as a continuous mixture of Poisson and Gamma distributions. Thus, a negative binomial random variable denoted as $x \sim \text{NB}(r, p)$ can be expressed as $x \sim \text{Poisson}(\lambda)$ where the rate parameter λ is also a Gamma-distributed random variable $\lambda \sim \Gamma(k, \theta)$, with $k = r$ and $\theta = \frac{p}{1-p}$.

Thus, let λ_l^C , $l = 1, 2, \dots, L$, be i.i.d. Gamma-distributed random rates corresponding to the Poisson-distributed number of visible clusters at any time instant for L different locations of the MS. Using the scaling property of the Gamma distribution and assuming that the L random rates are i.i.d. as $\lambda_l^C \sim \Gamma(k, \theta T_S/C)$ with C the total number of clusters, the aggregated number of visible clusters follows a negative binomial distribution, i.e., $n_C(t) \sim \text{NB}(r, p)$ with parameters $r = k$ and $p = \theta/(\theta + 1)$. The average of the aggregated number of visible clusters is given by $N_C = \mathbb{E}[n_C(t)] = \mathbb{E}[\lambda_l^C C/T_S] = k\theta$. Finally, using measured parameters p and r of the negative binomial distribution as given in [12], the random (dis)appearance rates can be modeled as i.i.d. random variables distributed as $\lambda_l^C \sim \Gamma(r, \frac{p}{1-p} \frac{T_S}{C})$. From the physical point of view, it is reasonable to expect different average numbers of visible clusters at different locations of the MS. This assumption is less restrictive than the opposite, i.e., that of spatially-invariant average number of visible clusters. The previous results focused on the temporal characteristics of the number of visible rays/clusters can be analogously extended to the spatial (array) domain and they are omitted here for brevity.

D. Observed Cluster Length and MPC Length Within Clusters

The observed cluster length and MPC length within clusters can be used to characterize cluster-level evolution and ray-level evolution over the array, respectively [21], [22]. The observed cluster length is defined as

$$L_{cluster} = \frac{I_s - I_e}{2} \quad (40)$$

where I_s and I_e denote the start index and end index in the array dimension, respectively. Similarly, the MPC length is defined as

$$L_{MPC} = \frac{I_{sn} - I_{en}}{2L_{cluster}} \quad (41)$$

where I_{sn} and I_{en} denote the start index and end index of the n -th ray in the cluster in the array dimension, respectively. Note that the MPC length within clusters is normalized by the cluster length $L_{cluster}$.

IV. RESULTS AND ANALYSIS

As the main contribution of this work is the ray-level spatial-temporal evolution process, in this section we will numerically study the effects produced by the ray-level gain on the statistical properties of the channel model. Since the

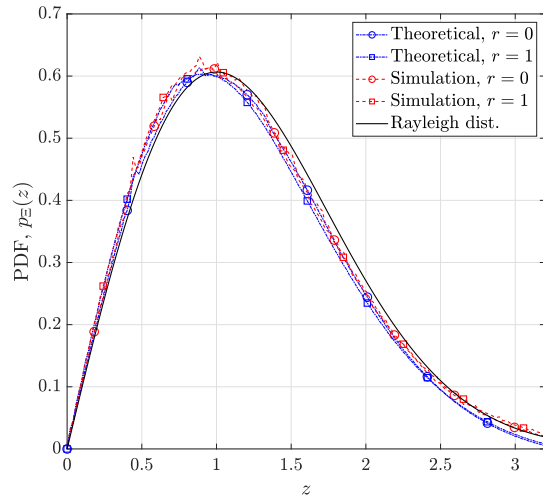


Fig. 3. Comparison of the theoretical and simulated distribution of the envelope for rapid and slow (dis) appearance times, i.e., $r = 0$ and $r = 1$, respectively. The Rayleigh distribution of unit variance is also shown for comparison ($\sigma = 1$, $N_a = 10$).

receive array is small and not subject to large-array propagation effects, the statistical properties of the channel model are the same for all elements of the receive array under the assumption that all antenna elements are equal. Therefore, only the results corresponding to a single receive antenna element are shown for clarity. The results allow to compare relevant statistical properties of the proposed channel model with those of the state-of-the-art massive MIMO channel models obtained without using ray-level evolutions as stated in Section I. The theoretical results were obtained by numerical evaluation of the expressions derived in Section III. For the Monte Carlo simulations, we used the recent massive MIMO channel measurements reported in [21], [22] to generate the channel parameters, e.g., ray-level visibility characteristics, angles, and delays, and computed 10^3 realizations of the CTF in (3). The measurements [21], [22] were conducted in a subway station, employing a virtual 256-element rectangular antenna array at the Tx side and a single antenna element at the Rx side. The sounding signals were centered at 6 GHz and spanned 100 MHz in [21] and at 11 GHz and spanned 200 MHz in [22]. Advanced clustering and tracking algorithms enabled the authors to obtain both cluster- and ray-level parameters and their evolution over the array, e.g., ray (dis)appearance rates. Although both Tx and Rx remained static due to the limitations of the virtual array technique, we will assume the Tx moves at a constant speed in order to study the ACF and Doppler spectrum predicted by the channel model.

A. Envelope Distribution

First, we will study the effect of the ray-level gain and its parameters on the distribution of the envelope as defined in Section III-A2. In Fig. 3, the distribution $p_{\Xi}(z)$ is depicted for short and long (dis)appearance times, i.e., for values of the taper parameter $r = 0$ and $r = 1$, respectively. For reference, the Rayleigh distribution of unit variance is also shown. Both theoretical and simulated distributions resemble a Rayleigh

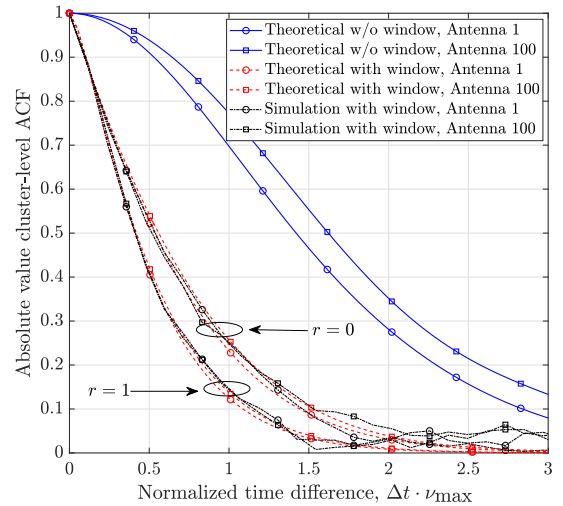


Fig. 4. Comparison of the absolute values of the theoretical and simulated ACFs with and without ray-level evolution for different values of the temporal taper parameter r ($N_a = 10$, $N_T = 256$, $N_R = 1$, $\alpha^T = 45^\circ$, $\beta^T = 0^\circ$, $\mathbf{s}_c^T = (4, 4, 0)$ m, $\phi_\mu^T = 45^\circ$, $\phi_\sigma^T = 4^\circ$, $\theta_\mu^T = 0^\circ$, $\theta_\sigma^T = 0.5^\circ$, $\alpha_v^T = 135^\circ$, $\beta_v^T = 90^\circ$, $\nu_{\max} = 24$ Hz, $\nu_{\max}^T \cdot T^R = 0.7$).

distribution almost independently of r . The root-mean-square error of the approximation of the simulation results to the theoretical ones is below 1% and that of the simulation results to the reference Rayleigh distribution is below 2%. However, note that the maximum amplitude of the rays is scaled by r as $c = \sigma \left[\frac{N_a}{2} (1 - \frac{5}{8}r) \right]^{-\frac{1}{2}}$ to compensate the reduction of amplitude caused by the taper. This is, the contribution of every ray to the overall received signal is uneven as the amplitude of every ray is weighted by the ray gain. In addition, it can be seen that the average number of visible rays required to achieve a given level of accuracy approximating a Rayleigh distribution is larger than that of existing models due to the random nature of the number of rays.

B. ACF

In Fig. 4, we present a comparison of the theoretical and simulated absolute values of the array-variant cluster-level ACFs with and without ray-level evolution for a maximum Doppler frequency of $\nu_{\max}^T = 24$ Hz. These results show that the ray-level evolution process can have a strong impact on the temporal correlation and hence the coherence time. As the average lifetime of rays is shorter than the cluster's coherence time, the ray-level evolution process significantly reduces the total cluster-level ACF. For instance, for a correlation level of 0.5, the coherence time becomes $1/\nu_{\max}^T$ seconds shorter in Fig. 4, which represents a reduction of 66% of the coherence time of the cluster without considering ray-level evolution.

The impact of the (dis)appearance times on the ACF is less significant than that of the rays' lifetimes, but its effects are not negligible. Long (dis)appearance times ($r \approx 1$) reduce the temporal ACF more than short ones ($r \approx 0$) because rays' lifetimes are independent of their duration, i.e., T_n^R does not increase with r . If the total lifetime of the ray depended on r , the effect would be the opposite. Note that we have used the spatial rays' lifespans D^R provided in [21] in order to calculate

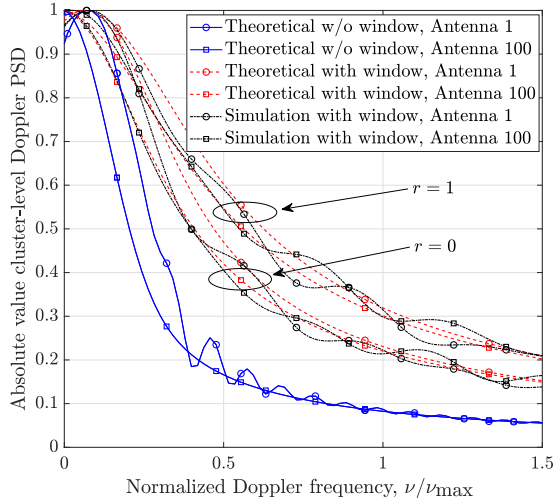


Fig. 5. Comparison of the absolute values of the theoretical and simulated cluster-level Doppler PSDs with and without ray-level evolution for different values of the temporal taper parameter r ($N_a = 10$, $N_T = 256$, $N_R = 1$, $\alpha^T = 45^\circ$, $\beta^T = 0^\circ$, $\mathbf{s}_c^T = (4, 4, 0)$ m, $\phi_\mu^T = 45^\circ$, $\phi_\sigma^T = 4^\circ$, $\theta_\mu^T = 0^\circ$, $\theta_\sigma^T = 0.5^\circ$, $\alpha_v^T = 135^\circ$, $\beta_v^T = 90^\circ$, $\nu_{\max} = 24$ Hz, $\nu_{\max}^T \cdot T^R = 0.7$).

the temporal lifespan as $T^R = D^R/v^T$. In addition, note that the ray-level evolution process reduces the differences among ACFs at different locations of the antenna array produced by near-field effects.

C. Doppler PSD

In Fig. 5, a comparison of the theoretical and simulated cluster-level Doppler PSDs is presented. Since the simulated Doppler PSD has been obtained through the Fourier transformation of the corresponding ACF, the effects of the ray-level evolution can be deduced by duality. Thus, a short average lifetime of rays leads to large cluster-level Doppler spreads. In particular, we observe in Fig. 5 that the cluster-level Doppler spread increases from 75 to 86 Hz on average, which represents a 15% approximately. In addition, shorter (dis)appearance times ($r \approx 0$) spread the Doppler PSD less than longer ones ($r \approx 1$). As explained above, this effect is due to the independence of the rays' lifetimes on r . Finally, note the differences in the Doppler spectra at different locations of the array that demonstrate the non-stationary properties of the channel in the spatial domain.

D. S-CCF

In Fig. 6, the theoretical and simulated absolute values of the cluster-level S-CCFs with and without ray-level evolution of the proposed model as well as the S-CCFs in [25] without ray-level evolution are compared. The consistency of the two models without ray-level evolution can further verify the correctness of the proposed model. The effects of the ray-level gain are similar to those observed above for the ACF. Thus, the small sizes of the rays' VRs tend to reduce the cluster-level antenna correlation. As presented in [21], the average lifespan of rays is one order of magnitude shorter than cluster's. This

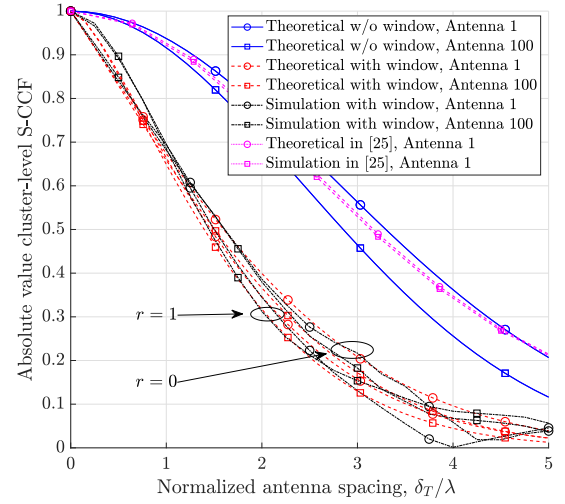


Fig. 6. Comparison of the absolute values of the theoretical and simulated cluster-level S-CCFs with and without ray-level evolution ($N_a = 10$, $N_T = 256$, $N_R = 1$, $\alpha^T = 0^\circ$, $\beta^T = 0^\circ$, $\mathbf{s}_c^T = (5, 5, 0)$ m, $\phi_\mu^T = 45^\circ$, $\phi_\sigma^T = 4^\circ$, $\theta_\mu^T = 0^\circ$, $\theta_\sigma^T = 6^\circ$, $R^R = 0.15$ (1.2 λ) m).

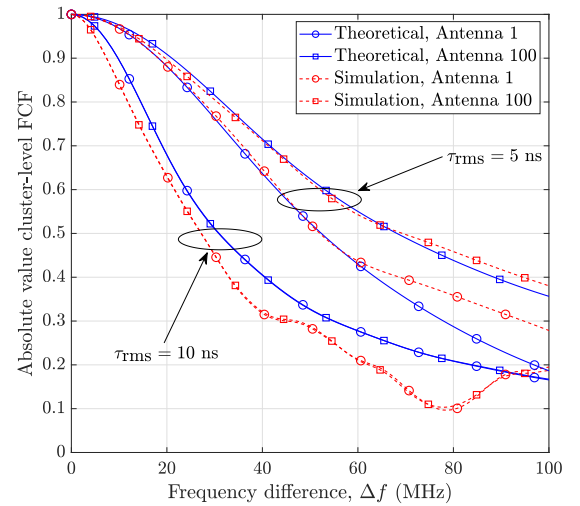


Fig. 7. Comparison of the absolute values of the theoretical and simulated cluster-level FCF for different values of intra-cluster delay spread ($N_a = 10$, $N_T = 256$, $N_R = 1$, $\alpha^T = 45^\circ$, $\beta^T = 0^\circ$, $\mathbf{s}_c^T = (4, 4, 0)$ m, $\phi_\mu^T = 45^\circ$, $\phi_\sigma^T = [6 \ 50]^\circ$, $\theta_\mu^T = 0^\circ$, $\theta_\sigma^T = [4 \ 30]^\circ$).

is specially important for clusters highly concentrated in the angular domain, since they present longer coherence regions. For widespread clusters in the angular domain, the effect of the ray-level evolution process is lower as the S-CCF decays faster. Note also that the effect of the parameter r on the S-CCF is smaller than that observed in the ACF above due to the 2D circular shape of the ray-level spatial VRs.

E. FCF

In Fig. 7 we present a comparison of the theoretical and simulated absolute values of the cluster-level FCFs. The FCF is unaltered by the ray-level gain as this is independent of the delay domain. However, note that the FCF depends on the antenna element considered as a consequence of the delay

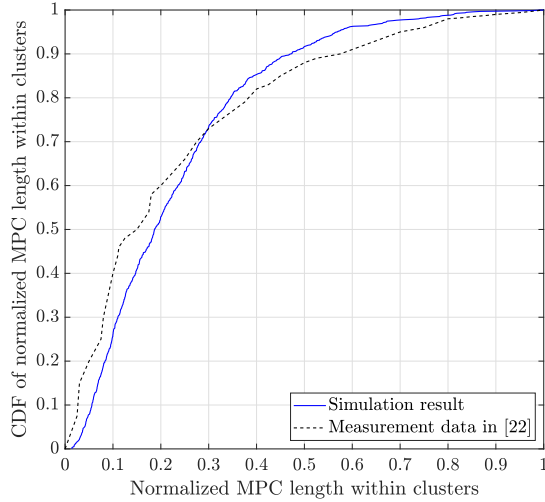


Fig. 8. Comparison of measured in [22] and simulated CDFs of the MPC length within clusters over the array ($N_T = 256$, $N_R = 1$, $\delta_H^T = 0.5\lambda$, $\delta_V^T = 0.5\lambda$).

drifts and spread, as described in [29]. These effects are more noticeable for values of the delay spread similar to the time it takes a ray to travel across the array, i.e., when $\tau_{\text{rms}} \approx c_0^{-1} \cdot D_A$, with D_A the largest dimension of the array.

F. Observed Cluster Length and MPC Length Within Clusters

Fig. 8 shows the cumulative distribution functions (CDFs) of the measured and simulated MPC length within clusters over the array. The abscissa axis of the figure is the normalized MPC length within clusters, as defined in Equation (41). The simulation results show a good agreement with the measurements data presented in [22].

V. CONCLUSION

In this paper, we have proposed a novel 3D space-time non-stationary wideband massive MIMO channel model that is able to capture ray-level near-field effects and smooth (dis)appearance in massive MIMO channels. Moreover, we have studied the impact of the ray-level evolution process on the most important statistical properties of the channel model and concluded that the cluster-level ACF, Doppler PSD, and S-CCF can be largely affected by the rays' lifespan. The smoothness of (dis)appearance has a relatively small impact on the statistical properties of the channel, which makes the tapered cosine function a good candidate due to its simplicity and flexibility. Additional measurement results may help select a more accurate function for the ray evolution process. A comparison of measured and simulated CDFs of the MPC length within clusters over the array have validated the ray-level evolution process. We have also proposed a method to determine the most adequate wavefront for each cluster and ray. A large percentage of clusters and rays of limited lifespan can still use plane wavefronts, which can significantly reduce the computational complexity of the channel model. The proposed channel model is a general one and can be applied to many different practical communication scenarios

with different statistical properties such as urban, rural, and indoor scenarios, by adjusting channel model parameters.

APPENDIX

DISTRIBUTION OF THE ENVELOPE

The distribution of Ξ can be calculated as [53]

$$p_{\Xi}(z) = (2\pi)^2 z \int_0^{\infty} \left[\prod_{n=1}^N \int_0^{\infty} p_{g_n}(y_n) J_0(2\pi y_n x) dy_n \right] \times J_0(2\pi z x) x dx. \quad (42)$$

Thus, plugging (11) into (42), we obtain

$$\begin{aligned} p_{\Xi}(z) &= (2\pi)^2 z \int_0^{\infty} \left(\prod_{n=1}^N \int_0^{c_n} [(1-p_v)\delta(y_n) \right. \\ &\quad \left. + \frac{p_v r}{\pi \sqrt{c_n y_n - y_n^2}} + p_v(1-r)\delta(y_n - c_n)] \right. \\ &\quad \left. \times J_0(2\pi y_n x) dy_n \right) J_0(2\pi z x) x dx \\ &= (2\pi)^2 z \int_0^{\infty} \prod_{n=1}^N [(1-p_v) + p_v(1-r)J_0(2\pi c_n x) \\ &\quad + \frac{p_v r}{\pi} \int_0^{c_n} \frac{J_0(2\pi y_n x)}{\sqrt{c_n y_n - y_n^2}} dy_n] J_0(2\pi z x) x dx \\ &= (2\pi)^2 z \int_0^{\infty} \prod_{n=1}^N [(1-p_v) + p_v(1-r)J_0(2\pi c_n x) \\ &\quad + p_v r {}_2F_3\left(\frac{1}{4}, \frac{3}{4}; \frac{1}{2}, 1, 1; -(c_n \pi x)^2\right)] \\ &\quad \times J_0(2\pi z x) x dx \end{aligned} \quad (44)$$

for $z > 0$ and with ${}_2F_3(\cdot; \cdot; \cdot)$ denoting the generalized hypergeometric series of order 2, 3 [47]. For the special case where all the windows have the same maximum amplitude $c = c_n$, then

$$\begin{aligned} p_{\Xi}(z) &= (2\pi)^2 z \int_0^{\infty} \{1 + p_v [{}_2F_3(1/4, 3/4; 1/2, 1, 1; \\ &\quad - (c\pi x)^2) r + J_0(2\pi c x)(1-r) - 1]\}^N \\ &\quad \times J_0(2\pi z x) x dx. \end{aligned} \quad (46)$$

As the number of active rays at time instant t is a Binomial-distributed random variable with N trials and probability of success $p_v = (\lambda^R T_C)^{-1}$, the average number of visible rays at any time instant is $N_a = N(\lambda^R T_C)^{-1}$. Thus, substituting $p_v = \frac{N_a}{N}$ into (46)

$$\begin{aligned} p_{\Xi}(z) &= (2\pi)^2 z \int_0^{\infty} \left\{1 + \frac{N_a}{N} [{}_2F_3(1/4, 3/4; 1/2, 1, 1; \right. \\ &\quad \left. - (c\pi x)^2) r + J_0(2\pi c x)(1-r) - 1]\right\}^N \\ &\quad \times J_0(2\pi z x) x dx. \end{aligned} \quad (47)$$

In the limit $N \rightarrow \infty$ and assuming that the average number of rays N_a is constant, we can use the well-known identity $e^x = \lim_{n \rightarrow \infty} (1 + x/n)^n$ in the integrand of (47) as

$$\begin{aligned} p_{\Xi}(z) &= (2\pi)^2 z \int_0^{\infty} \exp \left\{ N_a \left[{}_2F_3\left(\frac{1}{4}, \frac{3}{4}; \frac{1}{2}, 1, 1; \right. \right. \right. \\ &\quad \left. \left. - (c\pi x)^2) r + J_0(2\pi c x)(1-r) - 1 \right] \right\} \\ &\quad \times J_0(2\pi z x) x dx. \end{aligned} \quad (48)$$

REFERENCES

- [1] E. G. Larsson, O. Edfors, F. Tufvesson, and T. L. Marzetta, "Massive MIMO for next generation wireless systems," *IEEE Commun. Mag.*, vol. 52, no. 2, pp. 186–195, Feb. 2013.
- [2] C.-X. Wang *et al.*, "Cellular architecture and key technologies for 5G wireless communication networks," *IEEE Commun. Mag.*, vol. 52, no. 2, pp. 122–130, Feb. 2014.
- [3] X.-H. You *et al.*, "Towards 6G wireless communication networks: Vision, enabling technologies, and new paradigm shifts," *Sci. China Inf. Sci.*, vol. 64, no. 1, pp. 1–74, Jan. 2021, doi: [10.1007/s11432-020-2955-6](https://doi.org/10.1007/s11432-020-2955-6).
- [4] C. Shepard *et al.*, "Argos: Practical many-antenna base stations," in *Proc. ACM MOBICOM*, Istanbul, Turkey, Aug. 2012, pp. 53–64.
- [5] J. Vieira *et al.*, "A flexible 100-antenna testbed for massive MIMO," in *Proc. GC Wkshps*, Austin, TX, USA, Dec. 2014, pp. 287–293.
- [6] P. Harris *et al.*, "LOS throughput measurements in real-time with a 128-antenna massive MIMO testbed," in *Proc. IEEE GLOBECOM*, Washington, DC, USA, Dec. 2016, pp. 1–7.
- [7] D. Tse and P. Viswanath, *Fundamentals of Wireless Communication*, 1st ed. Cambridge, U.K.: Cambridge Univ. Press, 2005.
- [8] E. Björnson, J. Hoydis, and L. Sanguinetti, "Massive MIMO networks: Spectral, energy, and hardware efficiency," *Found. Trends Signals Process.*, vol. 11, nos. 3–4, pp. 154–655, 2017, doi: [10.1561/20000000093](https://doi.org/10.1561/20000000093).
- [9] C. A. Balanis, *Antenna Theory: Analysis and Design*, New York, NY, USA: Wiley, 2005.
- [10] S. Gregson, J. McCormick, and C. Parini, *Principles of Planar Near-Field Antenna Measurements*, 1st ed. London, U.K.: The Institution of Engineering and Technology, 2007.
- [11] X. Gao, F. Tufvesson, O. Edfors, and F. Rusek, "Measured propagation characteristics for very-large MIMO at 2.6 GHz," in *Proc. ASILOMAR*, Pacific Grove, CA, USA, Nov. 2012, pp. 295–299.
- [12] X. Gao, F. Tufvesson, and O. Edfors, "Massive MIMO channels—Measurements and models," in *Proc. ASILOMAR*, Pacific Grove, CA, USA, Nov. 2013, pp. 280–284.
- [13] S. Payami and F. Tufvesson, "Channel measurements and analysis for very large array systems at 2.6 GHz," in *Proc. IEEE EUCAP*, Prague, Czech Republic, Mar. 2012, pp. 433–437.
- [14] S. Payami and F. Tufvesson, "Delay spread properties in a measured massive MIMO system at 2.6 GHz," in *Proc. IEEE PIMRC*, London, U.K., Sep. 2013, pp. 53–57.
- [15] W. Li, L. Liu, C. Tao, Y. Lu, J. Xiao, and P. Liu, "Channel measurements and angle estimation for massive MIMO systems in a stadium," in *Proc. ICACT*, Seoul, South Korea, Jul. 2015, pp. 105–108.
- [16] A. O. Martinez, E. De Carvalho, and J. O. Nielsen, "Towards very large aperture massive MIMO: A measurement based study," in *Proc. GC Wkshps*, Austin, TX, USA, Dec. 2014, pp. 281–286.
- [17] X. Gao, O. Edfors, F. Rusek, and F. Tufvesson, "Massive MIMO performance evaluation based on measured propagation data," *IEEE Trans. Wireless Commun.*, vol. 14, no. 7, pp. 3899–3911, Jul. 2015.
- [18] X. Gao, O. Edfors, F. Tufvesson, and E. G. Larsson, "Massive MIMO in real propagation environments: Do all antennas contribute equally?" *IEEE Trans. Commun.*, vol. 63, no. 11, pp. 3917–3928, Nov. 2015.
- [19] J. Huang, C.-X. Wang, R. Feng, J. Sun, W. Zhang, and Y. Yang, "Multi-frequency mmWave massive MIMO channel measurements and characterization for 5G wireless communication systems," *IEEE J. Sel. Areas Commun.*, vol. 35, no. 7, pp. 1591–1605, Jul. 2017.
- [20] J. Chen, X. Yin, X. Cai, and S. Wang, "Measurement-based massive MIMO channel modeling for outdoor LoS and NLoS environments," *IEEE Access*, vol. 5, pp. 2126–2140, 2017.
- [21] J. Li *et al.*, "Cluster-based 3-D channel modeling for massive MIMO in subway station environment," *IEEE Access*, vol. 6, pp. 6257–6272, 2018.
- [22] J. Li, B. Ai, R. He, M. Yang, Z. Zhong, and Y. Hao, "A cluster-based channel model for massive MIMO communications in indoor hotspot scenarios," *IEEE Trans. Wireless Commun.*, vol. 18, no. 8, pp. 3856–3870, Aug. 2019.
- [23] C.-X. Wang, J. Huang, H. Wang, X. Gao, X. You, and Y. Hao, "6G wireless channel measurements and models: Trends and challenges," *IEEE Veh. Technol. Mag.*, vol. 15, no. 4, pp. 22–32, Dec. 2020.
- [24] S. Wu, C. X. Wang, H. Haas, E. H. M. Aggoune, M. M. Alwakeel, and B. Ai, "A non-stationary wideband channel model for massive MIMO communication systems," *IEEE Trans. Wireless Commun.*, vol. 14, no. 3, pp. 1434–1446, Mar. 2015.
- [25] S. Wu, C.-X. Wang, M. Aggoune, M. M. Alwakeel, and Y. He, "A non-stationary 3-D wideband twin-cluster model for 5G massive MIMO channels," *IEEE J. Sel. Areas Commun.*, vol. 32, no. 6, pp. 1207–1218, Jun. 2014.
- [26] S. Wu, C.-X. Wang, E.-H.-M. Aggoune, M. M. Alwakeel, and X. You, "A general 3-D non-stationary 5G wireless channel model," *IEEE Trans. Commun.*, vol. 66, no. 7, pp. 3065–3078, Jul. 2018.
- [27] A. O. Martinez, P. Eggers, and E. De Carvalho, "Geometry-based stochastic channel models for 5G: Extending key features for massive MIMO," in *Proc. PIMRC*, Valencia, Spain, Sep. 2016, pp. 1–6.
- [28] C. F. Lopez, C.-X. Wang, and R. Feng, "A novel 2D non-stationary wideband massive MIMO channel model," in *Proc. IEEE CAMAD*, Toronto, ON, Canada, Oct. 2016, pp. 207–212.
- [29] C. F. Lopez and C.-X. Wang, "Novel 3-D non-stationary wideband models for massive MIMO channels," *IEEE Trans. Wireless Commun.*, vol. 17, no. 5, pp. 2893–2905, May 2018.
- [30] T. R. 38.901, "Study on channel model for frequencies from 0.5 to 100 GHz," Tech. Rep. V14.3.0, 2017.
- [31] T. R. 38.901, "Preliminary draft new report ITURM.[IMT-2020.EVAL], test environments and channel models," 3GPP, Tech. Rep. TR 38.901, V14.3.0, Jun. 2017.
- [32] L. Raschkowski *et al.*, "METIS channel models (D1.4)," METIS Project, Tech. Rep. ICT-317669, Jul. 2015.
- [33] S. Jaekel, L. Raschkowski, K. Börner, and L. Thiele, "QuaDRiGa: A 3-D multi-cell channel model with time evolution for enabling virtual field trials," *IEEE Trans. Antennas Propag.*, vol. 62, no. 6, pp. 3242–3256, Jun. 2014.
- [34] X. Gao, J. Flordelis, G. Dahman, F. Tufvesson, and O. Edfors, "Massive MIMO channel modeling-extension of the COST 2100 model," in *Proc. JNCW Wkshps*, Barcelona, Spain, Oct. 2015, pp. 1–10.
- [35] M. Peter *et al.*, "Measurement campaigns and initial channel models for preferred suitable frequency ranges," mmMAGIC Project, Tech. Rep. D2.1 V1.0, 2016.
- [36] A. Maltev *et al.*, "Channel modeling and characterization," ICT FP7 MiWEBA Project, Tech. Rep. D5.1 V1.0, Jun. 2014.
- [37] J. Flordelis, X. Li, O. Edfors, and F. Tufvesson, "Massive MIMO extensions to the COST 2100 channel model: Modeling and validation," *IEEE Trans. Wireless Commun.*, vol. 19, no. 1, pp. 380–394, Jan. 2020.
- [38] J. Bian, C.-X. Wang, X. Gao, X. You, and M. Zhang, "A general 3D non-stationary wireless channel model for 5G and beyond," *IEEE Trans. Wireless Commun.*, vol. 20, no. 5, pp. 3211–3224, May 2021.
- [39] C. F. Lopez and C.-X. Wang, "A study of 2D non-stationary massive MIMO channels by transformation of delay and angular power spectral densities," *IEEE Trans. Veh. Technol.*, vol. 69, no. 12, pp. 14212–14224, Dec. 2020.
- [40] Y. Liu, C.-X. Wang, J. Huang, J. Sun, and W. Zhang, "Novel 3-D nonstationary mmWave massive MIMO channel models for 5G high-speed train wireless communications," *IEEE Trans. Veh. Technol.*, vol. 68, no. 3, pp. 2077–2086, Mar. 2019.
- [41] J. Wang, C.-X. Wang, J. Huang, H. Wang, and X. Gao, "A general 3D space-time-frequency non-stationary THz channel model for 6G ultra-massive MIMO wireless communication systems," *IEEE J. Sel. Areas Commun.*, vol. 39, no. 6, pp. 1576–1589, Jun. 2021.
- [42] Y. Zheng, L. Yu, R. Yang, and C.-X. Wang, "A general 3D non-stationary massive MIMO GBSM for 6G communication systems," in *Proc. IEEE WCNC*, Nanjing, China, Mar. 2021, pp. 1–6.
- [43] C.-X. Wang, S. Wu, L. Bai, X. You, J. Wang, and C.-L. I, "Recent advances and future challenges for massive MIMO channel measurements and models," *Sci. China Inf. Sci.*, vol. 59, no. 2, pp. 1–16, Feb. 2016, doi: [10.1007/s11432-015-5517-1](https://doi.org/10.1007/s11432-015-5517-1).
- [44] C.-X. Wang, J. Bian, J. Sun, W. Zhang, and M. Zhang, "A survey of 5G channel measurements and models," *IEEE Commun. Surveys Tuts.*, vol. 20, no. 4, pp. 3142–3168, 4th Quart., 2018.
- [45] M. Pätzold, *Mobile Radio Channels*, 2nd ed. West Sussex, U.K.: Wiley, 2012.
- [46] C. F. López and C.-X. Wang, "A study of delay drifts on massive MIMO wideband channel models," in *Proc. IEEE WSA*, Bochum, Germany, Mar. 2018, pp. 1–7.
- [47] I. S. Gradshteyn and I. M. Ryzhik, *Table of Integrals, Series, and Products*, 8th ed. London, U.K.: Academic, 2014.

- [48] A. Borhani, G. L. Stüber, and M. Pätzold, "A random trajectory approach for the development of nonstationary channel models capturing different scales of fading," *IEEE Trans. Veh. Technol.*, vol. 66, no. 1, pp. 2–14, Jan. 2017.
- [49] G. D. Durgin, *Space-Time Wireless Channels*, Upper Saddle River, NJ, USA: Prentice-Hall, 2002.
- [50] C.-L. J. Lam and T. Le-Ngoc, "Estimation of typical sum of lognormal random variables using log shifted gamma approximation," *IEEE Commun. Lett.*, vol. 10, no. 4, pp. 234–235, Apr. 2006.
- [51] N. B. Mehta, J. Wu, A. F. Molisch, and J. Zhang, "Approximating a sum of random variables with a lognormal," *IEEE Trans. Wireless Commun.*, vol. 6, no. 7, pp. 2690–2699, Jul. 2007.
- [52] A. Abdi and M. Kaveh, "On the utility of gamma PDF in modeling shadow fading (slow fading)," in *Proc. IEEE VTC*, Houston, TX, USA, May 1999, pp. 2308–2312.
- [53] M. Pätzold and G. Rafiq, "Sparse multipath channels: Modelling, analysis, and simulation," in *Proc. IEEE PIMRC*, London, U.K., Sep. 2013, pp. 30–35.



Carlos F. López received the B.Sc. and M.Sc. degrees in telecommunications engineering from the Technical University of Madrid, Spain, in 2011 and 2015, respectively, and the Ph.D. degree in wireless communications from Heriot-Watt University, Edinburgh, U.K., in 2019.

He was a Research Engineer with the Radio Communication Research Group, Technical University of Madrid, from 2011 to 2014, where he led the design and development of simulation tools for wireless channel modeling in 4G/LTE mobile communications networks, and carried out measurement campaigns for wireless channel characterization using broadband communication systems in Madrid Metro facilities. He was a Research Engineer with the Radio Access Group, Telefónica Research and Development, in 2015, where he was involved in the simulation of 5G wireless communication systems, including massive multiple-input multiple-output (MIMO) and millimeter-wave (mm-Wave) technologies, and testing of adaptive channel coding schemes using link-to-system models. From 2015 to 2019, he was a Marie Curie Fellow, Research Associate, and Ph.D. Candidate at Heriot-Watt University, where he developed channel models for massive MIMO systems. He has been with the Wireless Standards Team, MathWorks, Glasgow, U.K., since 2018, developing standard-compliant wireless communication tools for the 5G, LTE, and WLAN toolboxes. His research interests include wireless communications technologies, link and system modeling, and channel modeling.



Cheng-Xiang Wang (Fellow, IEEE) received the B.Sc. and M.Eng. degrees in communication and information systems from Shandong University, Jinan, China, in 1997 and 2000, respectively, and the Ph.D. degree in wireless communications from Aalborg University, Aalborg, Denmark, in 2004.

He was a Research Assistant with the Hamburg University of Technology, Hamburg, Germany, from 2000 to 2001, a Visiting Researcher with Siemens AG Mobile Phones, Munich, Germany, in 2004, and a Research Fellow with the University of Agder, Grimstad, Norway, from 2001 to 2005. He has been with Heriot-Watt University, Edinburgh, U.K., since 2005, where he was promoted to a Professor in 2011. In 2018, he joined Southeast University, Nanjing, China, as a Professor. He is currently a part-time Professor with Purple Mountain Laboratories, Nanjing. He has authored four books, three book chapters, and more than 430 papers in refereed journals and conference proceedings, including 25 highly cited papers. He has also delivered 22 invited keynote speeches/talks and nine tutorials in international conferences. His current research interests include wireless channel measurements and modeling, 6G wireless communication networks, and applying artificial intelligence to wireless communication networks.

Dr. Wang is a Member of the Academia Europaea (The Academy of Europe), and a fellow of the IET and the China Institute of Communication (CIC). He is currently an Executive Editorial Committee Member of the IEEE TRANSACTIONS ON WIRELESS COMMUNICATIONS. He has served as a TPC member, the TPC chair, and the general chair for more than 80 international conferences. He is a Highly-Cited Researcher recognized by Clarivate Analytics from 2017 to 2020. He received 12 Best Paper Awards from IEEE GLOBECOM 2010, IEEE ICCT 2011, ITST 2012, IEEE VTC 2013–Spring, IWCMC 2015, IWCMC 2016, IEEE/CIC ICC 2016, WPMC 2016, WOCC 2019, IWCMC 2020, and WCSP 2020. He also received the 2020 and 2021 "AI 2000 Most Influential Scholar Award Honorable Mention" in recognition of his outstanding and vibrant contributions in the field of the Internet of Things. He has served as an Editor for nine international journals, including IEEE TRANSACTIONS ON WIRELESS COMMUNICATIONS, from 2007 to 2009, IEEE TRANSACTIONS ON VEHICULAR TECHNOLOGY, from 2011 to 2017, and IEEE TRANSACTIONS ON COMMUNICATIONS, from 2015 to 2017. He was a Guest Editor of IEEE JOURNAL ON SELECTED AREAS IN COMMUNICATIONS, Special Issue on Vehicular Communications and Networks (a Lead Guest Editor), Special Issue on Spectrum and Energy Efficient Design of Wireless Communication Networks, and Special Issue on Airborne Communication Networks. He was also a Guest Editor for IEEE TRANSACTIONS ON BIG DATA, Special Issue on Wireless Big Data, and is a Guest Editor for IEEE TRANSACTIONS ON COGNITIVE COMMUNICATIONS AND NETWORKING, Special Issue on Intelligent Resource Management for 5G and Beyond. He is an IEEE Communications Society Distinguished Lecturer in 2019 and 2020.



Yi Zheng (Student Member, IEEE) received the B.Sc. degree from Dalian Maritime University, China, in 2016, and the M.Eng. degree from Southeast University, China, in 2019, where she is currently pursuing the Ph.D. degree with the National Mobile Communications Research Laboratory.

Her research interests are massive MIMO channel measurements and modeling and maritime communication channel characterization and modeling.